Supplemental Figures

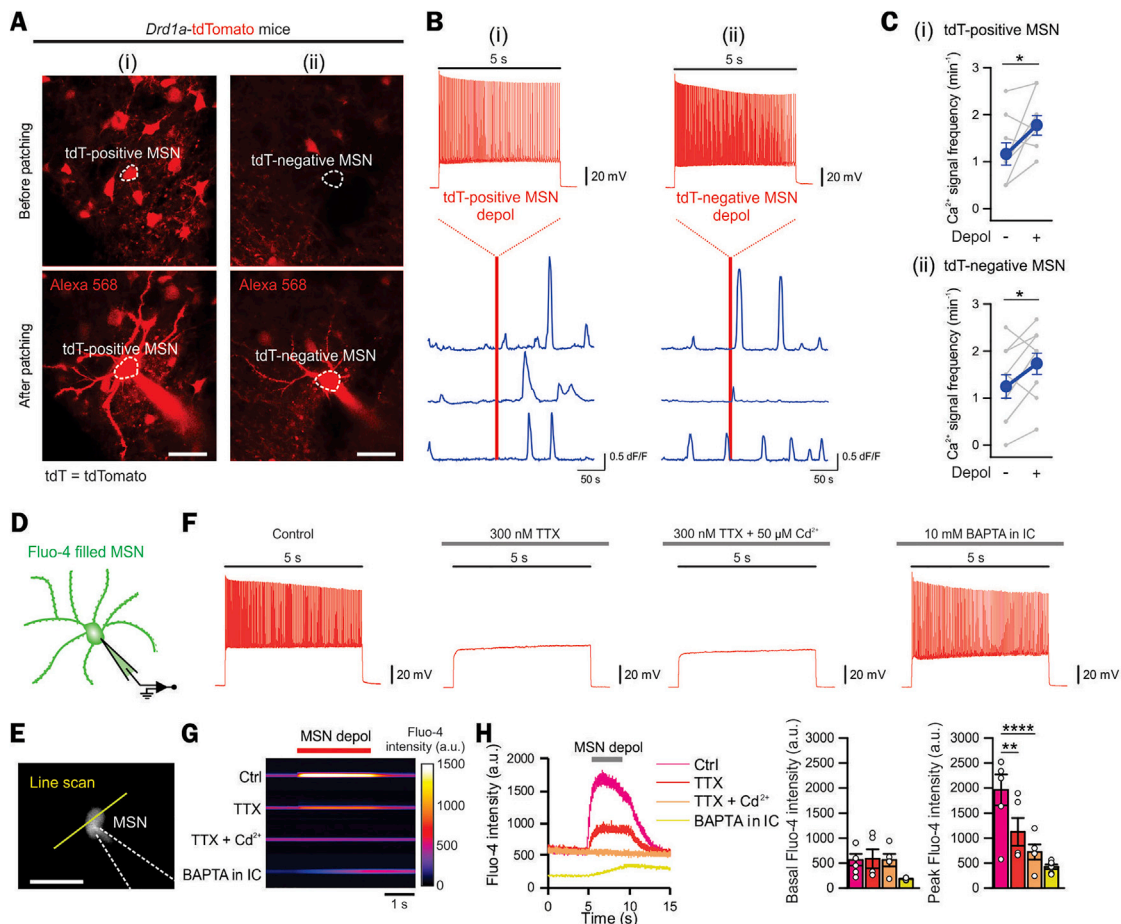**Figure S1. MSN Depolarization, which Induced Ca²⁺ Influx into MSNs, Activated Astrocyte Ca²⁺ Signaling Irrespective of MSN Subtypes, Related to Figure 1**

(A) Representative images showing tdTomato-positive (i, D1) and tdTomato-negative (ii, D2) MSNs from *Drd1a*-tdTomato mice before and after whole-cell patching (dialyzed with Alexa 568). (B) Depolarization of D1 or D2 MSNs to upstate like levels (96 ± 21 action potentials in i and 130 ± 6 action potentials in ii) increased the frequency of astrocyte Ca²⁺ signals (3 representative cells for each). (C) Astrocyte Ca²⁺ signal frequency before and after D1 or D2 MSN depolarization (n = 4 mice per group). ≥ 20% increase in Ca²⁺ signal frequency was observed in 7 out of 9 astrocytes (i) and 7 out of 10 astrocytes (ii). (D-E) Simultaneous electrophysiological recording and "fast" line scan intracellular Ca²⁺ imaging from MSNs filled with Fluo-4 via the patch pipette. (F) Representative traces from a MSN during depolarizing current injections (400 pA). MSNs displayed no action potentials (AP) in the presence of 300 nM TTX (with or without Cd²⁺) in the bath. However, intracellular BAPTA dialysis did not block MSN APs. (G) Representative line scan data of MSN intracellular Ca²⁺ levels before, during and after somatic depolarization (400 pA current injections). (H) The left graph shows representative traces for MSN intracellular Ca²⁺ line scan imaging data under the various conditions shown. The right bar graphs summarize average data from such experiments for basal and peak Fluo-4 intensity (n = 5-6 MSNs from 3-5 mice). Overall, in these experiments MSN-depolarization evoked intracellular Ca²⁺ elevations in MSNs were not abolished by TTX, but were abolished by bath application of Cd²⁺ and by BAPTA dialysis. Paired t test between before (basal) and after MSN depol (C). One-way ANOVA test (F). Scale bars, 20 μm (A) and 40 μm in (E). Data are shown as mean ± s.e.m. Full details of n numbers, precise *P values* and statistical tests are reported in Table S1. * indicates p < 0.05, ** indicates p < 0.01, **** indicates p < 0.0001.
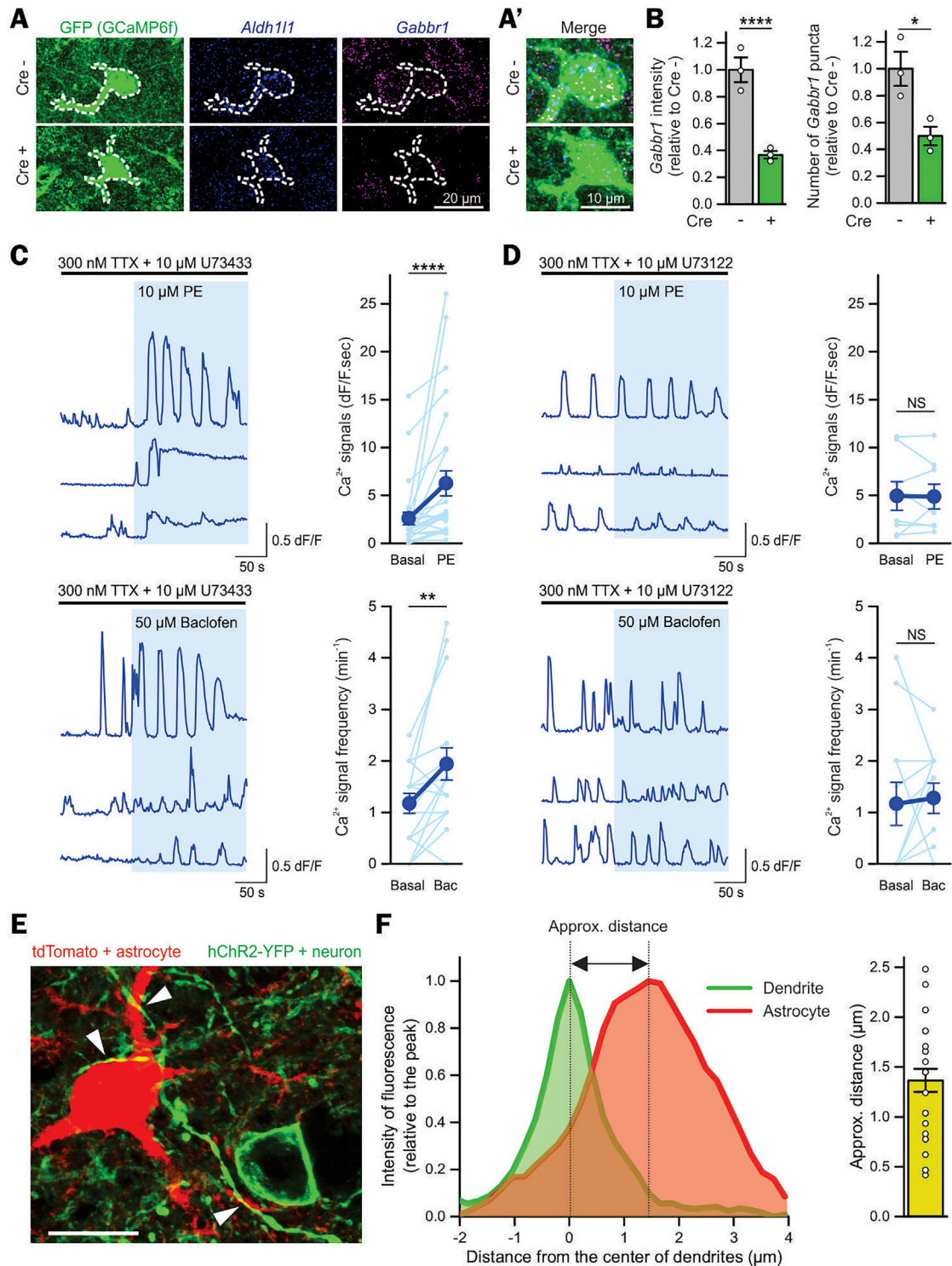
Figure S2. *Gabbr1* Deletion in Striatal Astrocytes, Intracellular Mechanism, and Proximity of Striatal Astrocytes to MSNs, Related to Figure 1

(A) To delete *Gabbr1* from striatal astrocytes, floxed *Gabbr1* mice received an AAV2/5 GfaABC$_1$D for selectively expressing Cre in astrocytes (AAV Cre+) along with GCaMP6f. Control mice were floxed *Gabbr1* mice that received only astrocyte selective AAV2/5 GCaMP6f (AAV Cre-). Representative images for *in situ* hybridization (RNAscope) for *Gabbr1* and *Aldh1l1* followed by IHC using anti-GFP antibodies to visualize GCaMP6f expressing astrocytes (outlined by dotted lines). (B) Average data of fluorescence intensity and puncta number of *Gabbr1* revealed with RNAscope showing its reduction in striatal astrocytes. n = 32-33 astrocytes from 3 mice. Unpaired t test (B). Scale bars, 20 μm (A) and 10 μm (A'). Data are shown as mean ± s.e.m. Full details of n numbers, precise *P value*s and

statistical tests are reported in Table S1. * indicates p < 0.05, **** indicates p < 0.0001. (C, D) PLC-dependent astrocyte Ca^{2+} signaling evoked by PE and baclofen. (C) 10 μM U73122, a PLC inhibitor, blocked PE and baclofen-evoked increases in striatal astrocyte Ca^{2+} signals (D), while 10 μM U73433, a control analog for U73122, did not (C). The traces shown are from 3 representative cells in each case and the scatter graphs are average data. n = 8-20 astrocytes from 3-4 mice. Wilcoxon signed ranks test (A, B). Data are shown as mean ± s.e.m. Full details of n numbers, precise *P value*s and statistical tests are reported in full in Table S1. ** indicates p < 0.01, NS indicates not significantly different. (E, F) MSN dendrites were juxtaposed with astrocyte somata and processes. (E) Representative image of a tdTomato-expressing astrocyte and YFP-expressing neuronal soma and dendrites in the striatum showing close apposition of astrocytes and MSN dendrites (arrows). (F) Average line-profile data showing the distance between the center of the dendrite and the center of the astrocyte somata and/or processes. The scatter graph reports average data from analyses such as those in b (n = 26 images, 4 mice). Scale bar, 20 μm (A). Data are shown as mean ± s.e.m.
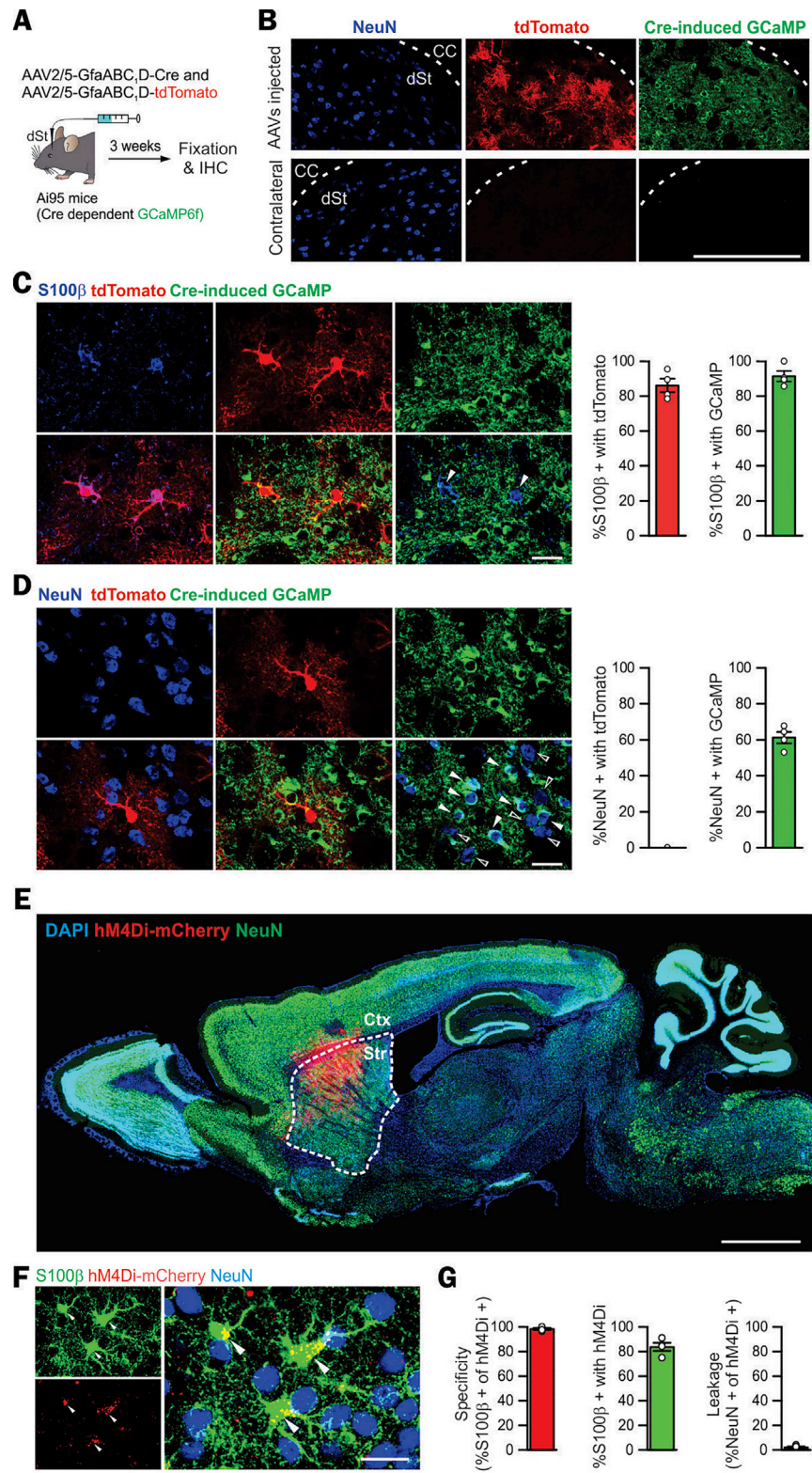
Figure S3. Gene Expression Using *GfaABC₁D* AAV2/5 in the Dorsal Striatum, Related to Figures 1 and 2

(A) Cartoon illustrating AAV2/5 microinjection into the dorsal striatum to express GCaMP6f by delivering AAV2/5 *GfaABC₁D*-Cre into Ai95 mice that have a floxed-STOP cassette preventing expression of GCaMP6f. AAV2/5 *GfaABC₁D*-tdTomato was co-injected. (B) Images showing tdTomato and GCaMP6f were expressed

in the dorsal striatum (dSt) which is underneath the corpus callosum (CC) in the AAVs-injected side, but not in the contralateral side. (C) Representative image of S100β positive astrocytes that express tdTomato and are GCaMP positive (arrows). Bar graphs show that 86% of the S100β positive astrocytes were tdTomato positive (red bar graph) and that 91% of the S100β positive astrocytes were GCaMP6f positive due to Cre (green bar graph). This indicates both AAVs were delivered into most of astrocytes in dSt. n = 4 mice. (D) Representative image showing that NeuN positive neurons did not express tdTomato which was driven under the $GfaABC_1D$ promoter. However, although Cre expression was driven under the same promoter, some NeuN positive neurons were GCaMP6f positive (arrows). Open arrows indicate GCaMP6f negative neurons. Bar graphs show that none of the NeuN positive neurons were tdTomato positive (left bar graph), but that 61% of the NeuN positive neurons were GCaMP6f positive (green bar graph). n = 4 mice. (E) Image of the brain distribution of hM4Di-mCherry, which was restricted to the striatum when AAV2/5 $GfaABC_1D$ hM4Di-mCherry was microinjected in the dorsal striatum. (F) Representative image of hM4Di-mCherry positive striatal astrocytes (arrows) that were S100β positive and NeuN negative. (G) Bar graphs show that 98% of the hM4Di-mCherry positive astrocytes were S100β positive (red bar graph). Furthermore, ∼84% of the S100β positive astrocytes in the dorsal striatum expressed hM4Di-mCherry (green bar graph) following AAV2/5 microinjections. However, an insignificant number of the hM4Di-mCherry positive cells were NeuN positive (∼2%; right bar graph). Taken together, these data indicate that AAV2/5 $GfaABC_1D$ mediated delivery of hM4Di-mCherry to the dorsal striatum was astrocyte selective and targeted most of the striatal astrocytes. n = 4 mice. Scale bars, 200 μm in panel (B), and 20 μm in panel (C),(D) and F, 2 mm in (E). Data are shown as mean ± s.e.m.

Additional note on *Gabbr1* f/f mice and AAV2/5 $GfaABC_1D$-Cre in relation to panels A-D: In data reported in the main text, we deleted GB1R from astrocytes using striatal AAV2/5 $GfaABC_1D$-Cre microinjections. We could identify astrocytes based on their bushy morphologies as well as by marker expression (Figures S2A and S2B), and we could therefore easily monitor the consequences of deleting GB1Rs in single cell evaluations. However, we could not use *Gabbr1* f/f mice for astrocyte-selective evaluations of more complex phenomena such as animal behavior. There are two reasons. First, there is no Cre mouse line that targets only striatal astrocytes, and thus crossing *Gabbr1* f/f mice with even the best available *Aldh1l1*-Cre/ERT2 mice would delete GB1Rs from all astrocytes in the CNS, and from all *Aldh1l1*-expressing cells in the periphery (Chai et al., 2017; Srinivasan et al., 2016). Such an approach would not allow meaningful assessment of astrocyte GB1Rs functions for striatum-dependent behaviors. Second, we could not use AAV2/5 $GfaABC_1D$-Cre microinjections, because as reported previously these viruses lead to low-level Cre expression within striatal neurons, which was sufficient to cause excision of floxed genomic sequences (Srinivasan et al., 2016). It is important to note, however, that the AAV2/5 $GfaABC_1D$ constructs do not lead to expression of other cargo such as reporters, channels and receptors in neurons (e.g., GFP, tdTomato, Kir4.1, DREADDS and GCaMP). For these molecules, the AAVs are demonstrably astrocyte selective (Adamsky et al., 2018; Anderson et al., 2016; Bonder and McCarthy, 2014; Cui et al., 2018; Haustein et al., 2014; Jiang et al., 2016; Jiang et al., 2014; Octeau et al., 2018; Rungta et al., 2016; Shigetomi et al., 2013; Srinivasan et al., 2015, 2016; Stobart et al., 2018; Tong et al., 2014; Yu et al., 2018). The explanation is that for such cargo to be measurably functional requires quite high expression, which the tropism of AAV2/5 and the $GfaABC_1D$ promoter favors for astrocytes, but prevents for neurons. However, in the case of Cre expression, even a very low number of recombinase molecules are sufficient to cause excision of floxed genomic sequences, resulting in observable effects in both neurons and astrocytes, as previously shown (Srinivasan et al., 2016). We report a specific set of experiments in panels A-D to document that the AAV constructs were astrocyte selective for reporter expression, but not for Cre-mediated excision of genomic sequences. Reporter expression was observed in 86 ± 4% of astrocytes and no neurons (0%), but Cre-mediated excision was observed in 91 ± 3% of astrocytes and 61 ± 3% of striatal neurons (C-D, n = 4 mice for each). For these reasons, we could not use the *Gabbr1* f/f mice to evaluate reliably astrocyte GB1R contributions to mouse behavior. We emphasize that these limitations of AAV2/5 $GfaABC_1D$-Cre apply to the striatum and hippocampus (Srinivasan et al., 2016). In the future, it may be possible to develop intersectional genetic approaches to target striatal astrocytes in the adult brain for selective gene deletion experiments.
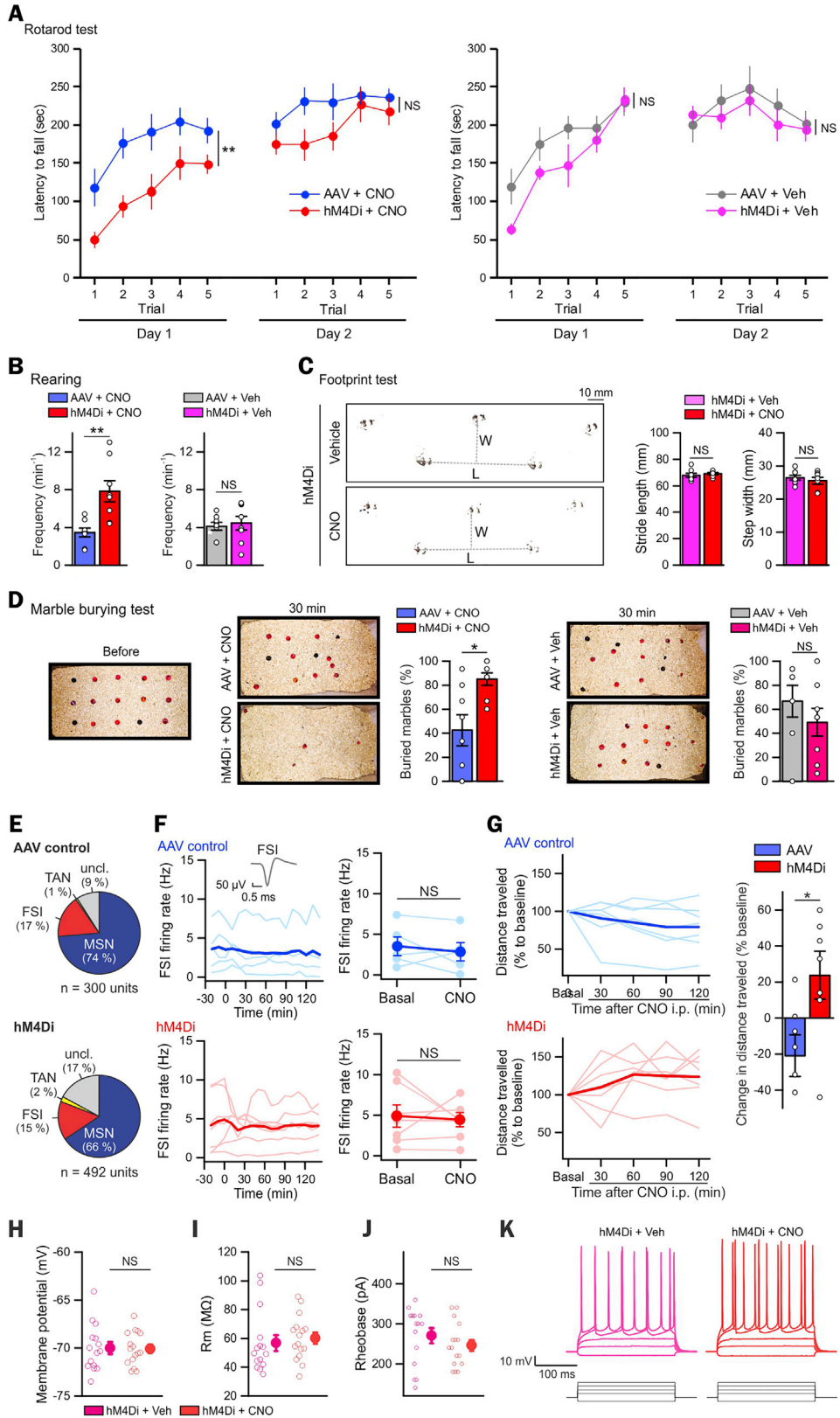
Figure S4. Additional Assessments of the Consequences of Astrocyte Gi Signaling *In Vivo*, Related to Figures 3 and 4

(A) Time spent on the accelerating Rotarod for individual trials completed at days 1 and 2 (5 trials per day). Note that there was a trend for the hM4Di + CNO mice to fall off the Rotarod sooner than the controls on Day 1, but this did not reach statistical significance at Day 2. We suspect this trend occurred because the mice appeared to rear more on the Rotarod on Day 1 and during this inattentive period they fell off. Consistent with this, panel (B) shows significantly increased rearing in the hM4Di + CNO group relative to controls. (C) Representative raw data for footprint tracks of mice walking on paper with their rear paws painted with black paint. The bar graphs show average data for footprint length and width, which is a measure of gate. (D) Marble burying test following activation of astrocyte Gi signaling. The number of buried marbles was significantly greater in the hM4Di + CNO group compared to AAV + CNO group. This is because the hM4Di + CNO group displayed hyperlocomotion (see main text), which resulted in greater disturbance of the bedding in the cage and thus more buried marbles n = 7-8 mice per group. (E) The pie charts show the types of neurons that were recorded with *in vivo* silicon probes in AAV control and hM4Di mice. TAN = tonically active neurons, FSI = fast spiking interneurons, MSN = medium spiny neurons, uncl = unclassified neurons. (F) Graphs show that the FSI firing rate was not altered after CNO i.p. administration at t = 0 min in hM4Di mice (7 mice) and control mice (5 mice). The inset shows a mean spike waveform of a representative FSI. (G) The graphs plot the distance that head-restrained mice traveled on a spherical treadmill before and following i.p. CNO administration. The distance was binned in 30 min blocks and normalized to the distance traveled in the 30 min before CNO i.p. injection (basal). Data from each mouse is shown in light traces, whereas the average data are shown in dark traces. The bar graph on the right summarizes the experiments and shows that hM4Di-expressing mice displayed significantly increased ambulation compared to control AAV-expressing mice. (H-K) Whole-cell current-clamp recordings from MSNs near hM4Di-expressing astrocytes following *in vivo* i.p. CNO administration revealed that the resting membrane potential (H), membrane resistance (I) and rheobase (J, K) of MSNs were not altered by activation of astrocyte Gi signaling under conditions that did later behavior as reported in the main manuscript. The right panels show representative traces from whole-cell current-clamp MSN recordings (current injections: -100, 100, 200, 300 and 400 pA). n = 15-16 MSNs from 4 mice. Two-way ANOVA test (A). Unpaired t test (B, D, G). Paired t test (F). Data are shown as mean ± s.e.m. Full details of n numbers, precise *P value*s and statistical tests are reported in Table S1. * indicates p < 0.05, ** indicates p < 0.01, NS indicates not significantly different.
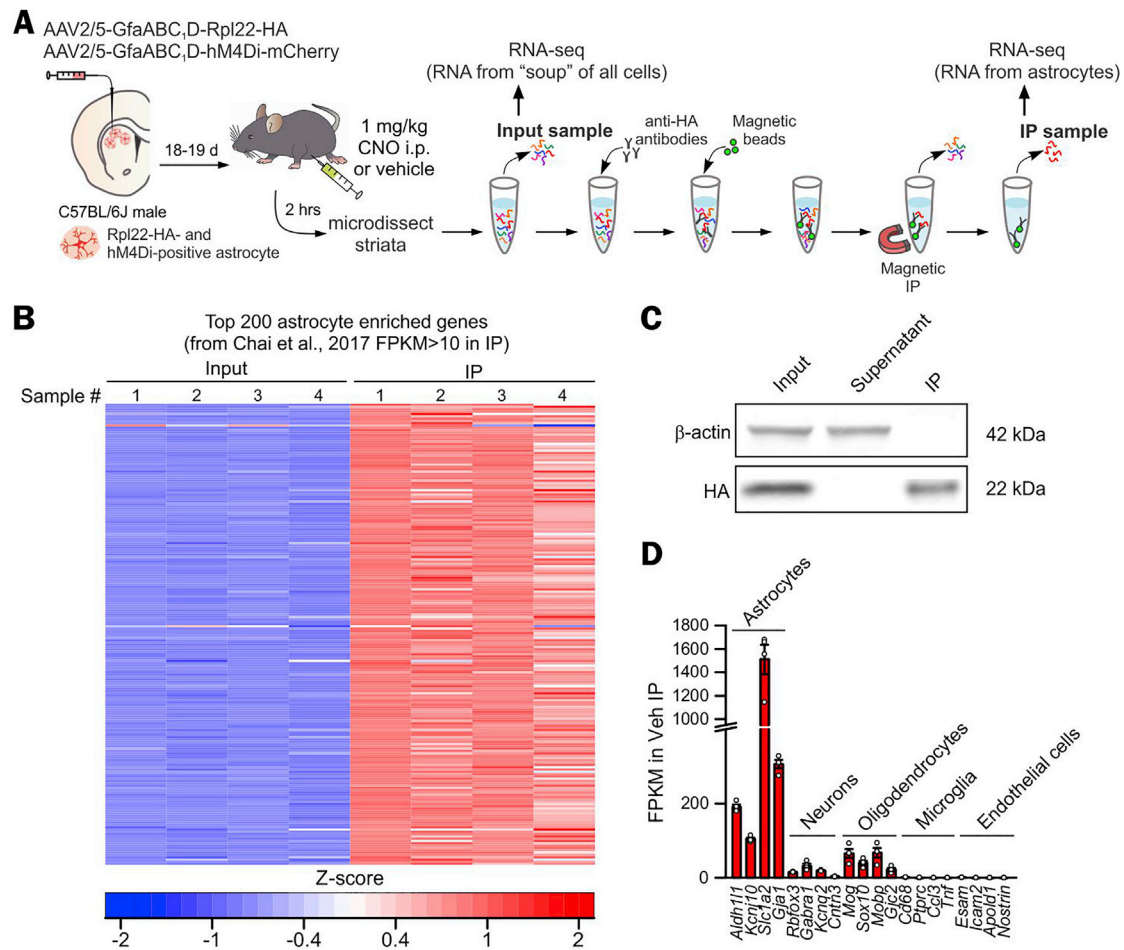
Figure S5. Astrocyte Transcriptomes from Adult Mouse Striatum following Astrocyte Gi Signaling Activation *In Vivo* for 2 h, Related to Figure 5

(A) Cartoon illustrating the experimental design employing AAV2/5 GfaABC$_1$D Rpl22-HA and the outline of the protocol for RNA-seq (Yu et al., 2018). (B) Heatmap showing relative enrichment (red) or depletion (blue) of the top 200 adult striatal astrocyte markers. Results from eight RNA-seq samples for both input and IP from four mice that received astrocyte specific hM4Di in the dorsolateral striatum are shown. The row Z scores were calculated using the FPKM values. These data show that the RNA-seq data were replete with known astrocyte markers, which served to validate the approach. (C) Representative western blot showing that Rpl22-HA was preserved in the IP sample, whereas β-actin was depleted in the IP sample (in relation to input). In contrast, Rpl22HA was not evident in the supernatant, whereas β-action was. n = three biological replicates. (D) Gene expression levels of cell-specific markers for astrocytes, neurons, oligodendrocytes, and microglia in IP samples from the hM4Di + Veh group. n = 4 mice per group. Data are shown as mean ± s.e.m All the RNA-seq data are provided the Table S2.
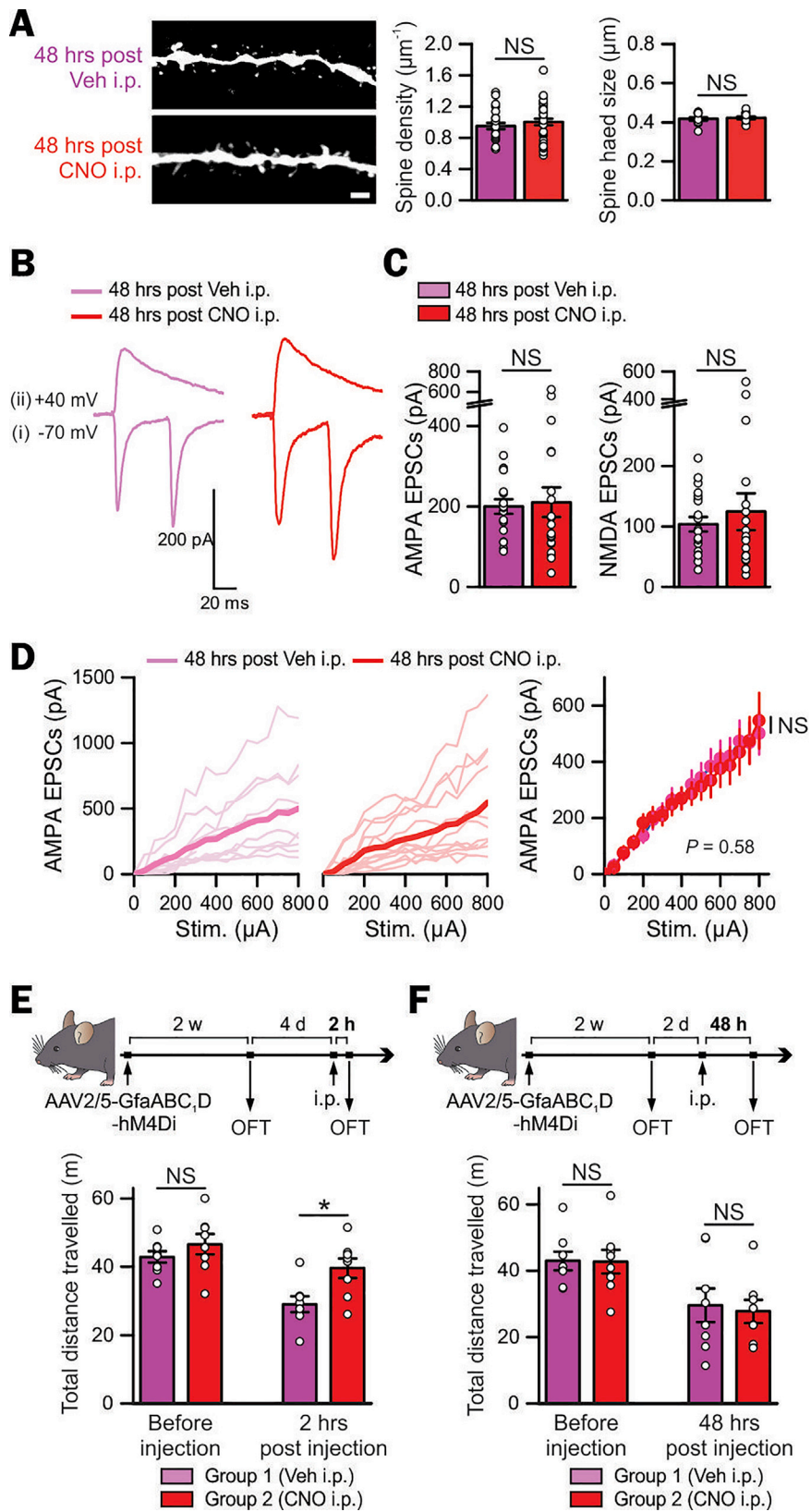
Figure S6. Astrocyte Gi Signaling-Mediated Changes Returned to Baseline 48 h after *In Vivo* CNO Administration, Related to Figures 3, 4, and 6

(A) Images on the left show spines from biocytin filled MSNs. Right two graphs show no significant difference in spine density and spine head size of MSNs in the indicated 2 experimental groups at 48 hr after CNO (n = 4 mice per group). (B) Representative traces for evoked AMPA EPSCs due to paired stimuli at membrane potentials of –70 mV (i) and for NMDA EPSCs due to single stimuli at +40 mV (ii) from the two indicated experimental groups. (C) Summary of multiple experiments such as those illustrated with representative traces in panel B (n = 20 MSNs from 4 mice). There was no significant change in EPSC amplitudes. (D) The two graphs on the left plot the AMPA EPSC amplitudes with multiple stimulation intensities to the cortico-striatal pathway in brain slices from the two indicated experimental groups. Plots in light colors show individual data from each MSN and those in dark colors indicate averaged data. The right graph show averaged plots from the two indicated experimental groups. (E) Cartoon illustrating the AAV2/5 reagents and approaches for selectively expressing hM4Di-mCherry bilaterally in striatal astrocytes. Once such mice were prepared, open field test (OFT) was performed twice: (i) 2 weeks after AAV surgery (before injection) and (ii) 2 hr after intra-peritoneal (i.p.) injection of 1 mg/kg CNO or vehicle. Bar graphs show that distance traveled by the mice over 30 min in an open field chamber for the 2 experimental groups. The distance traveled was not different between groups before i.p. injection. At 2 hr after i.p. injection, the CNO injected group showed hyperactivity compared to the vehicle injected group. n = 8 mice per group. (F) Cartoon illustrating the AAV2/5 reagents and approaches for selectively expressing hM4Di-mCherry bilaterally in striatal astrocytes. OFT was performed twice: (i) 2 weeks after AAV surgery and (ii) 48 hr after i.p. injection of 1 mg/kg CNO or vehicle. Bar graphs show that distance traveled by the mice over 30 min in an open field chamber. The distance traveled was not different between groups before and after i.p. injection. n = 8 mice per group. Thus, the statistically significant effects observed at 2 hr after CNO abated by 48 hr. Mann-Whitney test or unpaired Student's t test as appropriate (A,C,E,F). Two-way ANOVA repeated-measure followed by Tukey's post hoc test (D). Scale bar, 2 μm (A). Data are shown as mean ± s.e.m. Full details of n numbers, precise *P value*s and statistical tests are reported in Table S1. * indicates p < 0.05, NS indicates not significantly different.
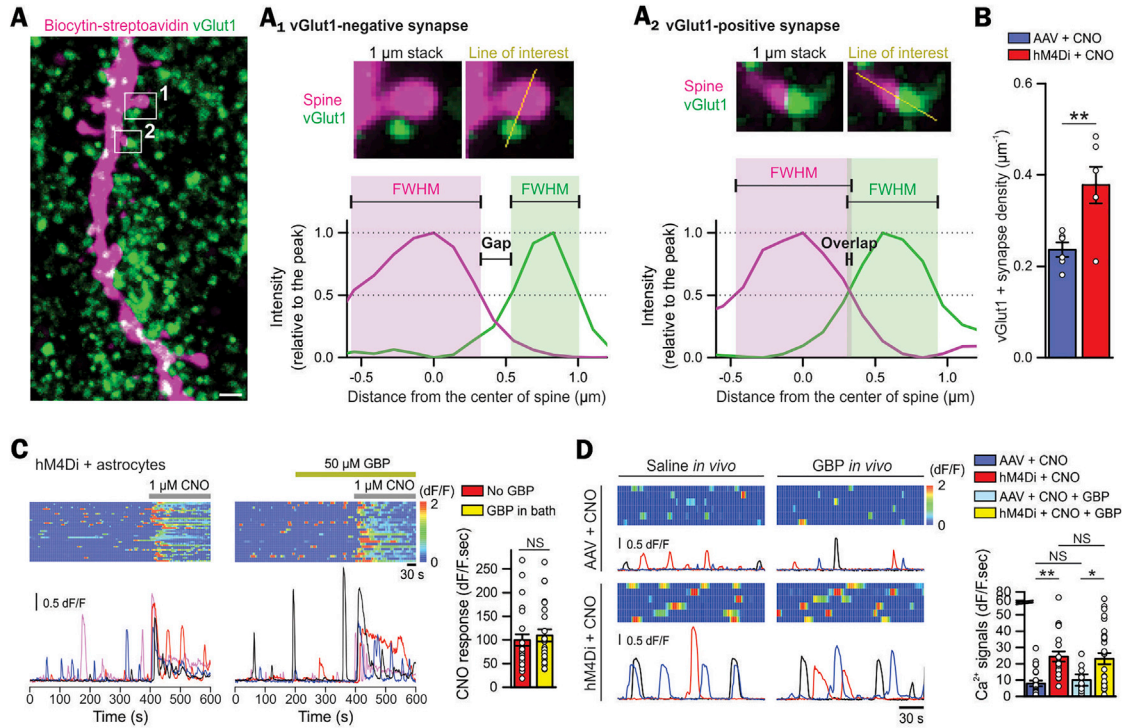
Figure S7. Activation of Astrocyte Gi Signaling Increased vGlut1-Positive Synapses onto MSNs, and Gabapentin Did Not Alter Astrocyte Ca^{2+} Signals Mediated by Gi Signaling, Related to Figure 6

(A) Representative image of a dendritic shaft and dendritic spines of a MSN filled with biocytin via intracellular dialysis during whole-cell recordings, in relation to vGlut1 + puncta. Such images were used to assess synapses. Putative synapses for the open squares 1 and 2 are shown in A$_1$ and A$_2$, respectively. A$_1$ and A$_2$ illustrate how we defined vGlut1-positive or negative synapses (see STAR Methods for detail). Briefly, vGlut1 positive synapses were defined as such if the vGlut1 and dendritic spine fluorescence signals overlapped at the full-width half maxima of the cognate optical signals from line profile analyses. The outcome of this analysis showed that 47 ± 6% of MSN dendritic spines formed vGlut1 positive synapses in control mice (n = 138-177 spines from 6 MSNs from 3 mice), which is similar to previous work on MSNs (Doig et al., 2010). (B) Summary graph shows that astrocyte Gi signaling activation resulted in increased vGlut1-positive synapses onto MSNs relative to the control group (6 MSNs, mice). (C) Kymographs and ΔF/F traces of astrocyte Ca^{2+} responses before and during bath application of 1 μM CNO in the absence or presence of 50 μM Gabapentin in the bath. The bar graph shows the CNO-evoked astrocyte Ca^{2+} signals (integrated area) with and without Gabapentin in bath (n ≥ 25 cells from 4 mice). (D) Kymographs and ΔF/F traces of astrocyte Ca^{2+} responses. The bar graphs summarize the integrated areas of the spontaneous astrocyte Ca^{2+} signals in hM4Di and control mice that received either Gabapentin or saline i.p. 3 hr prior, and CNO i.p. 2 hr prior to dissection (n ≥ 22 astrocytes from 4 mice). These data show that a single *in vivo* dose of CNO evoked a long lasting increase in astrocyte Ca^{2+} signaling and *in vivo* Gabapentin administration did not alter the CNO response. Unpaired t test (B). Mann-Whitney test (C). Two-way ANOVA followed by Tukey's post hoc test (D). Scale bar, 2 μm (A). Data are shown as mean ± s.e.m. Full details of n numbers, precise *P value*s and statistical tests are reported in Table S1. * indicates p < 0.05, ** indicates p < 0.01, NS indicates not significantly different.